3

Solidification Modeling of Single-Crystal Investment Castings

K. O. Yu
M. J. Beffel
M. Robinson
PCC Airfoils, Inc., Beachwood, Ohio
D. D. Goettsch
B. G. Thomas
University of Illinois, Champaign, Illinois
D. Pinella
Structural Dynamics Research Corp., Milford, Ohio
R. G. Carlson
GE Aircraft Engines, Cincinnati, Ohio

ABSTRACT

Single-crystal superalloys provide the metal temperature capability for gas turbine airfoils. These parts are manufactured by the unidirectional withdrawal solidification method. The final casting integrity depends upon their structures as well as inherent defects, which are determined during solidification. Efforts were undertaken in the MANTECH program and at PCC Airfoils to correlate the solidification conditions and the microstructures and defects of single-crystal castings. The approach combines finite-element thermal analysis and experimental results. Clusters of instrumented cast cylinders with various diameters, core sizes, core materials and shroud sizes were formed at specified furnace temperatures and withdrawal rates.

A finite-element model, developed to analyze thermal conditions during casting, generated data on cooling rates, local solidification times, thermal gradient (G) and solidification velocity (R). Results show that the finite-element thermal analysis can accurately model the casting process with relatively short computer run times. Moreover, correlations of casting microstructures and defects with calculated solidification conditions indicate this finite-element modeling is a powerful tool for predicting microstructures and defects in single-crystal investment castings.

INTRODUCTION

Because single-crystal superalloys provide the highest metal temperature capability[1] for gas turbine airfoils, the past decade has seen the increasing specification of directionally solidified and single-crystal turbine components in advanced propulsion systems. These parts are manufactured by the undirectional withdrawal investment casting process (Figs. 1 and 2).

Directional solidification is accomplished in a vacuum by pouring molten alloy into a ceramic mold preheated above the alloy's liquidus temperature. (Molds preheated to a temperature below the liquidus temperature result in "equiaxed grains," as shown in Figure 3A.) Solidification proceeds in a directional manner as a consequence of the thermal gradient created between the upper molten alloy (maintained by a heating coil) and the bottom water-cooled copper chill plate, which is extracting heat by contact with the hot metal.

After solidification has started, the ceramic mold filled with molten superalloy is gradually withdrawn from the heated furnace, and heat loss is now controlled by radiation from mold to the cold

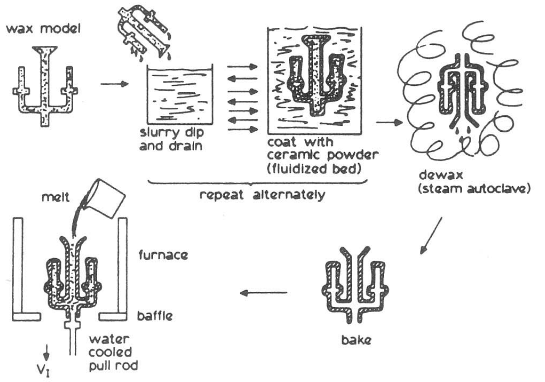

Fig. 1. Schematic illustration of the stages during the manufacture and use of investment molds for directional solidification.[2]

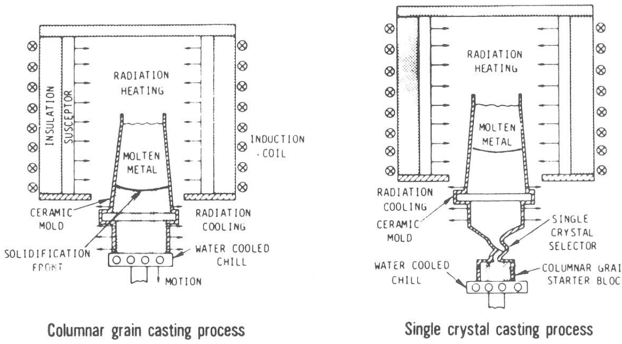

Columnar grain casting process

Single crystal casting process

Fig. 2. Schematic drawing of directional solidification process for columnar-grained and single-crystal turbine blades.[3]

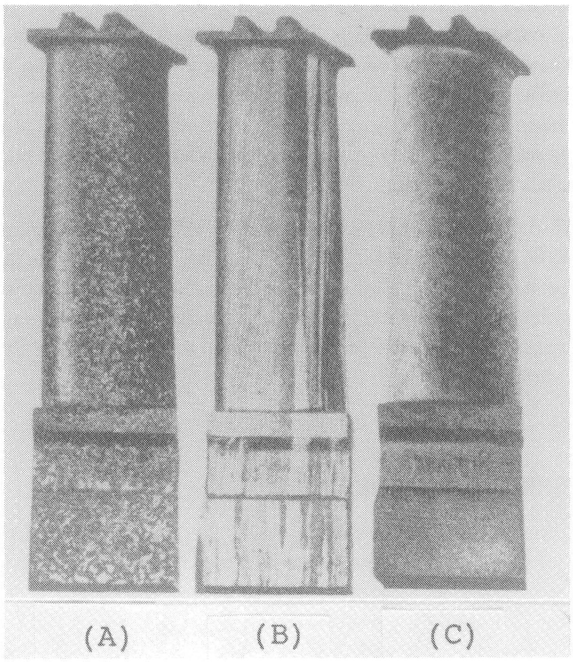

Fig. 3. Grain structures (equiaxed grains [A], columnar grains [B] and single-crystal [C]) in turbine airfoils.[2]

vacuum chamber walls. The initial columnar grain structure in the starter block proceeds to fill the entire mold cavity resulting in a columnar grain airfoil (Fig. 3B). A single-crystal casting is obtained by inclusion of a "grain selector" or single-crystal seed above the "starter" block, which permits only a single grain to pass through (Fig. 3C).

The final casting integrity depends upon its internal structure as well as inherent defects, both of which are determined during solidification. As a result of the increasing specification of turbine components in jet engines, engine manufacturers have increased their demands on the investment casting industry to establish highly reliable manufacturing processes to manufacture these components with controlled solidification conditions.

The use of traditional foundry engineering techniques to develop manufacturing processes have not always yielded optimum processes. This is because these traditional techniques have been based largely on empirical methods, intuitive experimentation, and keen observation of the response of the solidifying casting to variations in process variables.

It is generally not possible to reliably predict, given a turbine component's geometry, its course of solidification from inspection. As a consequence, much time is spent in attempting to find a process that can economically produce the casting, even if it is not optimum. The result is that the shipped casting costs more than it would if an ideal process were developed, high startup costs are incurred, and casting quality, though high enough to meet the demanding specifications of engine manufacturers, has not achieved its ultimate level.

Finite-element thermal modeling offers the capability of simulating casting solidification. Past work has centered on sand castings,[4] roll castings,[5] and investment casting of equiaxed turbine components.[6] This work has demonstrated excellent agreement between predicted behavior and casting results. However, the current work focuses on single-crystal simulations and defect prediction.

In this light, useful information such as the cooling rate, local solidification time, temperature gradient (G), and solidification rate (R) can be calculated by the model at every position and time during casting. Defect maps based on G versus R can then be established to predict the evolution of microstructures and the occurrence of solidification-based casting defects. Using this information, the foundry engineer can be aided in specifying a casting process that may produce airfoils with desired mechanical properties as well as high yields.

Efforts were undertaken in the Air Force/GE Aircraft Engines MANTECH program and at PCC Airfoils, Inc., to establish a method to simulate the solidification of single-crystal castings. The approach combines finite-element thermal analysis and experimental verification. The purpose of this paper is to report the results from these studies.

EXPERIMENTAL PROCEDURE

Experimental investment casting molds were designed with two major objectives: 1) the generation of a broad range of solidification defects to serve as a database of information for modeling, and 2) provide a geometry suitable for quick finite-element model generation and rapid model turnaround to allow numerical testing of defect hypotheses. To fulfill these objectives, clusters of cylindrically-shaped bars with various diameters, core sizes, core materials, and shroud sizes were cast at specified furnace temperatures and withdrawal speeds. Thermocouples (Fig. 4) were placed in the mold, metal, core, and the grain selector to record the temperature as a function of time at specified locations. After shakeout of the mold, all heat-treated castings were inspected by grain etching, FPI (fluorescent penetrant inspection), X ray, and Laué X ray for defects such as porosities, hot tears, secondary/multigrains, equiaxed/recrystallized grains, freckles, slivers, and misaligned primary dendrite directions. The untreated pieces were used to measure the primary and secondary dendrite arm spacings and the size of the as-cast gamma prime precipitates.

FINITE-ELEMENT MODELING

Figure 5 shows the procedure for finite-element modeling of single-crystal castings. Metal and core geometries can be generated by commercially available software packages such as IDEAS and PATRAN. The mesh for the ceramic mold around the metal is semi-automatically generated through the use of EXTRUDE program of IDEAS. This extrusion is essential, since a typical finite-element casting model may contain up to 88% mold elements. The time savings in generating the mold over hand generation is significant.

The single-crystal casting process incorporates a withdrawal rate to control the solidification front. This withdrawal must be modeled as a time-changing radiation on the surface of the mold. The University of Illinois Materials Processing Consortium, in

Fig. 4. Experimental cluster with thermocouples.

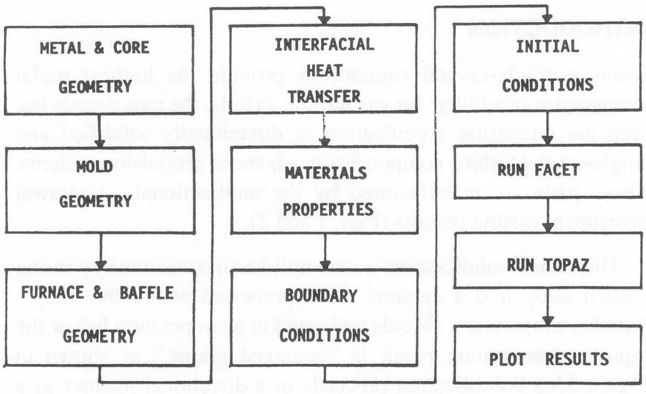

Fig. 5. Procedure for solidification modeling of single-crystal castings.

cooperative effort with Structural Dynamics Research Corporation (SDRC) and PCC Airfoils, developed the method of implementing this moving boundary condition.

To calculate the geometric view factors necessary for this simulation, SDRC modified FACET (Lawrence Livermore National Laboratory software) to work with TOPAZ/SDRC (a highly modified version of the Lawrence Livermore National laboratory TOPAZ/3D). The calculation requires that furnace and baffle geometries be added to the finite-element model. The transient heat conduction problem, including the time-dependent moving-boundary conditions, is solved by TOPAZ/SDRC (using the FACET output), to calculate temperature development under varying withdrawal conditions.

The interfacial heat transfer coefficients that are needed between the metal/mold, metal/core, metal/copper-chill, and mold/copper-chill interfaces are calculated by an inverse-heat-transfer method, based on the thermocouple data from the experimental clusters.

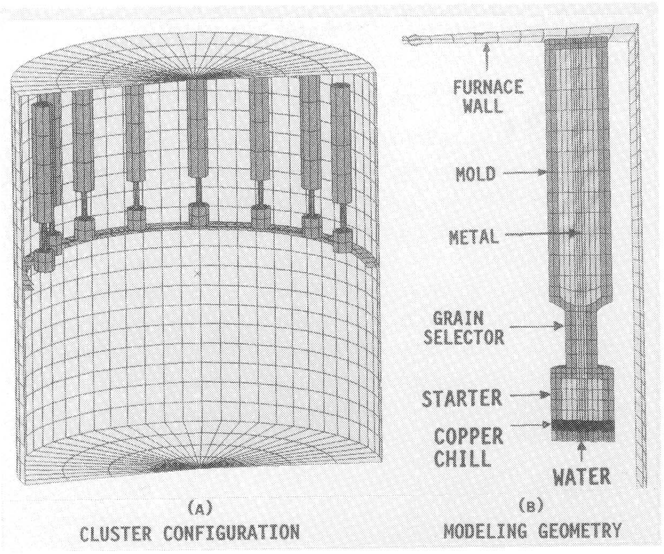

Fig. 6. Modeling configuration of the experimental clusters.

Thermophysical material properties of the alloy, mold, and core at temperatures up to 2800F were measured by TRW Electronics and Defense. Accurate determination of these values is essential in correctly modeling the casting solidification.

The finite-element solution is obtained by TOPAZ/SDRC and results available to the foundry engineer include isotherms, isochrons (time to reach the specified temperature), temperature gradients (G), solidification rates (R), combinations of G and R, cooling rates, local solidification times, heat fluxes, and cooling curves. These results are calculated by SDRC proprietary software and are displayed by IDEAS (Super TAB).

Figure 6A shows the modeling configuration of the experimental cluster shown in Figure 4. The geometry that is used to build the finite element model is shown in 6B. The symmetry of the cluster configuration permitted only half of a single bar to be modeled. For geometric simplicity, a cylinder of equivalent cross-sectional value was used to simulate the complex shape of the helical grain selector that is commonly used in the foundry.

RESULTS AND DISCUSSION

The validity of the modeling results and the effects of operating conditions on casting solidification behaviors are illustrated first. The evolution of casting microstructures and the occurrence of casting defects are then correlated with calculated solidification conditions. A defect map for the prediction of these defects is also constructed.

Modeling Results

The geometry used for the analysis is shown in Figure 6B. Cooling curves of three nodes that are located at the center of the cylinder and 0.25, 3, and 6 in. from the bottom of the starter are shown in Figure 7. As expected, because of the chill effect from the copper plate, the lower node (33) cools much faster than nodes located far from the chill (700 and 105).

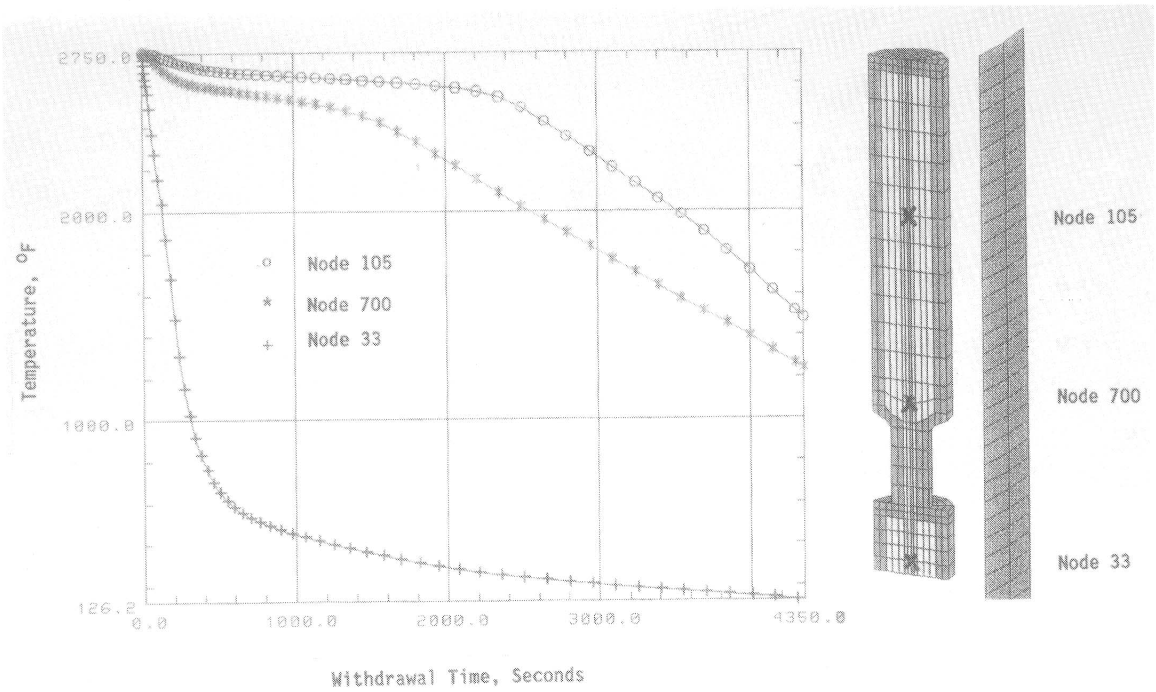

Fig. 7. Calculated cooling curves of three nodes at the center of the cylinder and 0.25, 3, and 6 inches from the bottom of the starter.

Cooling curves of three nodes that are located on the outer side, at the center, and the inner side of the cylinder are shown in Figure 8. It can be seen that the temperature of Node 203, which is located at the mold surface that is close to the furnace wall, is initially higher than the temperature of Node 105 (metal) and 1411 (located at the mold surface that is facing cluster center). When these nodes move below the baffle, the outer node (203) starts facing a cold furnace wall, and hence, cools much faster than the center (Node 105) and the inside (Node 1411). Consequently, the outside temperature is lower than that of the center (Node 105) and the inside (Node 1411). On the other hand, Node 1411 always faces other cylinders and the cold bottom plate of the cluster. Thus, its temperature is initially lower than that of Nodes 105 and 203. However, when these nodes move below the baffle, Node 1411 does not face the cold furnace wall, and, hence, it remains at a higher temperature than that of the outside cylinder (Node 203).

Figure 8 also shows the thermocouple data recorded at the center of the cylinder (Node 105). It can be seen that for most of the time (including the time in the critical solidification or mushy region, i.e., between 2606F and 2475F), the calculated cooling curve and thermocouple data are closely notched. The big discrepancy between the experimentally measured temperature data and the finite-element model predicted temperature (when the withdrawal time is smaller than 1200 seconds) is believed to be due to error in the thermocouple measurements. In fact, only in the upper chamber of the furnace does the thermocouple data diverge (for this TC, for times 0–1200 sec).

Calculated isotherms in a solid cylinder at various total withdrawal times are shown in Figure 9. It can be seen that, as expected, the location of the "mushy zone" (the partially solidified portion between liquidus and solidus temperatures) gradually moves from the bottom of the starter toward the top of the cylinder as the cylinder gradually withdraws from the baffle. The size of the mushy zone also increases with the total withdrawal time.

The metal pouring temperature and the furnace hot zone temperature are two operating parameters having important effects on casting solidification. In both the experimental clusters and these simulation models, the metal pour temperatures are the same as the furnace hot zone temperature. Figure 10 shows the isotherms within two cylinders cast at the same withdrawal speed but different metal pour temperatures.

It can be seen that the cylinder cast at a higher temperature has a smaller mushy zone than that of the cylinder cast at a lower pour temperature. This occurs because a higher metal pour temperature results in a higher temperature gradient in the mushy region, and hence, a smaller mushy zone size.

Figure 10 also shows that the mushy zone location of the cylinder cast at a higher pour temperature is closer to the starter; that is, most of the mushy zone is out of the furnace and below the baffle. This higher metal pour temperature results in a larger temperature difference between the pour temperature and the metal liquidus temperature. It therefore takes longer for the metal with a higher pour temperature to cool to the liquidus temperature; consequently, the mushy zone is prolonged farther beyond the furnace baffle.

The withdrawal speed is another operating parameter having an effect on casting cooling conditions. Figure 11 shows that at three inches from the bottom of the starter, the cylinder cast at a higher withdrawal speed cools faster than the cylinder cast at a lower withdrawal speed, since it leaves the furnace sooner. The corresponding local solidification time, based on these cooling curves, are 740 and 900 seconds, respectively. The cooling curve of nodes at six inches from the bottom of the starter show similar results. However, for those nodes that are near the bottom of the starter the effects of the withdrawal speed are negligible, due to rapid cooling.

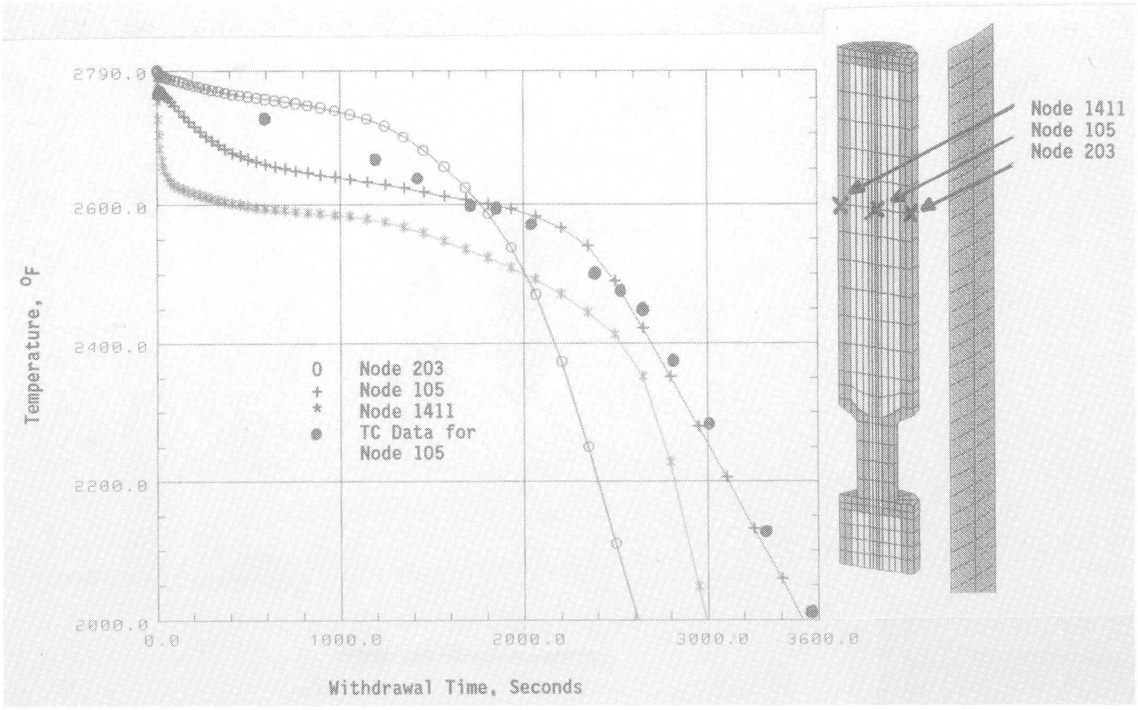

Fig. 8. Calculated cooling curves of three nodes at 6 inches from the bottom of the starter.

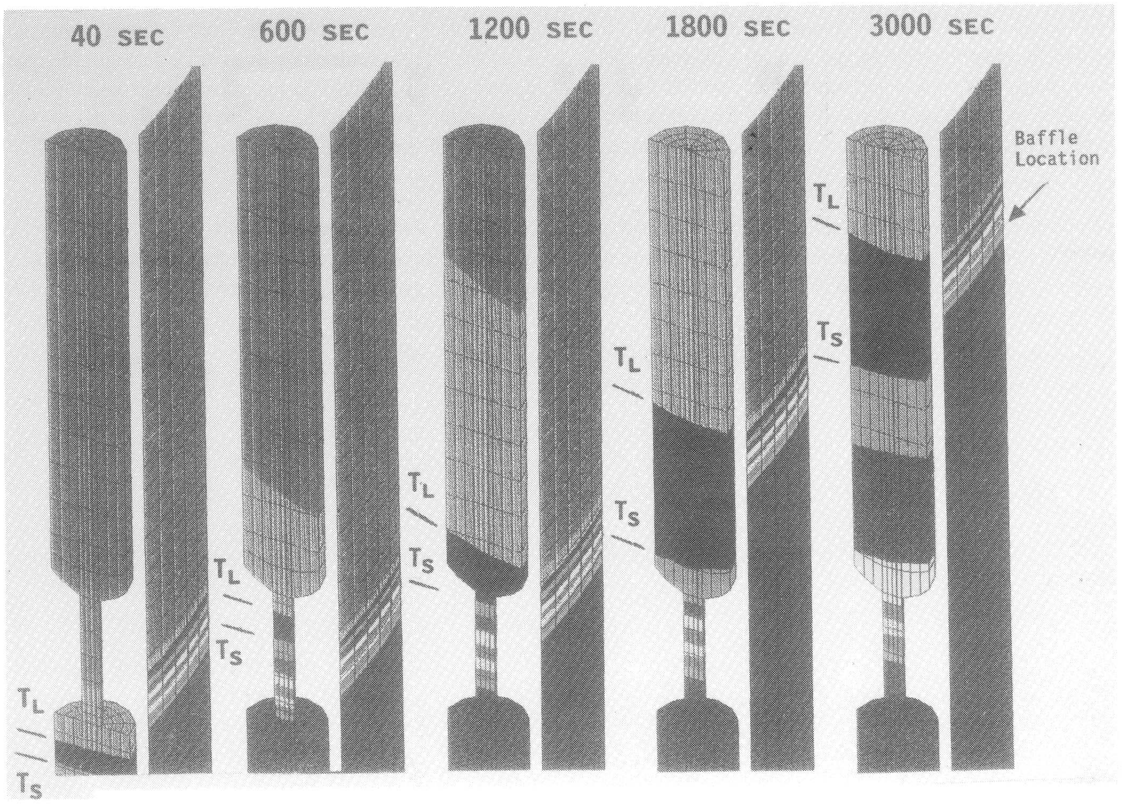

Fig. 9. Calculated isotherms of a solid cylinder at various total withdrawal times.

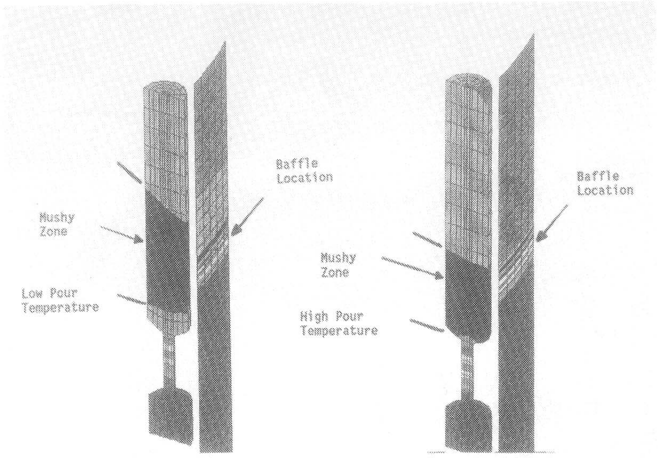

Fig. 10. Calculated isotherms of cylinders cast at different pour temperatures.

Correlation of Casting Microstructures and Defects with Solidification Conditions

Metallographically characterized casting microstructures and defects are now correlated with the calculated solidification conditions. A defect map, based on temperature gradient (G) and solidification rate (R), are constructed to predict the occurrence of the defects. Discussed next is the evolution of microstructures, the occurrence of casting defects (including freckles, recrystallized grains, shrinkage, slivers, etc.), the predicted defect map, and finally the off-axis prediction for the primary dendrite direction.

Evolution of Microstructures

The microstructural parameters evaluated are dendrite arm spacings (primary and secondary) and the as-cast gamma prime size. Two important parameters representing casting cooling conditions are: 1) local solidification time and 2) the time for metal to cool from a temperature of 2350F to 2000F (at which primary gamma prime will form), which can be calculated from the cooling curves shown in Figures 7 and 8. The relationship of dendrite arm spacing to local solidification time as well as the relationship of as-cast gamma prime size to the time for the solid metal to cool can then be obtained.

As-Cast Gamma Prime Size

Figure 12A shows the as-cast gamma prime precipitate size as a function of cooling rate of the single-crystal alloy for cooling from 2350F to 2000F. For the purpose of comparison, IN713C data from Bhambri et al.[7] are also shown in the figure. It can be seen that for IN713C, for high values of cooling rate, the as-cast gamma prime size increases with decreasing cooling rate. At low cooling rates, however, the gamma prime size appears to be independent of the cooling rate. Piearcey et al.[8] also noted a similar constancy of gamma prime dimensions with varying cooling rates in MarM200. For the single-crystal alloy, the as-cast gamma prime size is independent of cooling rates in the range of 0.3–7°F/sec. Figure 12B shows micrographs of as-cast gamma prime of the single-crystal materials at two different cooling rates.

Figure 12A also shows that the as-cast gamma prime size of single-crystal material is about twice of that of IN713C (an equiaxed alloy). This is believed to be due to the differences in chemical compositions and gamma prime solvus temperatures between these two alloys. In general, single-crystal alloys have higher aluminum and titanium (gamma prime forming elements) contents than equiaxed alloys. A higher aluminum and titanium content results in a higher alloy total gamma prime volume fraction, as well as a higher probability for a larger individual gamma prime size. A higher gamma prime solvus temperature means a higher diffusion rate for gamma prime precipitation and, hence, also results in a larger gamma prime size.

Single-crystal superalloys are given a solution heat treatment[1] at a temperature that is above the gamma prime solvus temperature to dissolve the as-cast gamma prime, and below the incipient melting temperature to prevent melting. Thus, the alloy gamma prime solution heat treatment temperature can be used as an indicator of the alloy gamma prime solvus temperature. This solution heat treatment temperature for a typical single-crystal alloy is about 2360F, compared with 2150F for IN713C.[9]

Dendrite Arm Spacing

For dendritic solidification, dendrite arm spacing (DAS) is the most convenient parameter for representing the degree of microsegregation

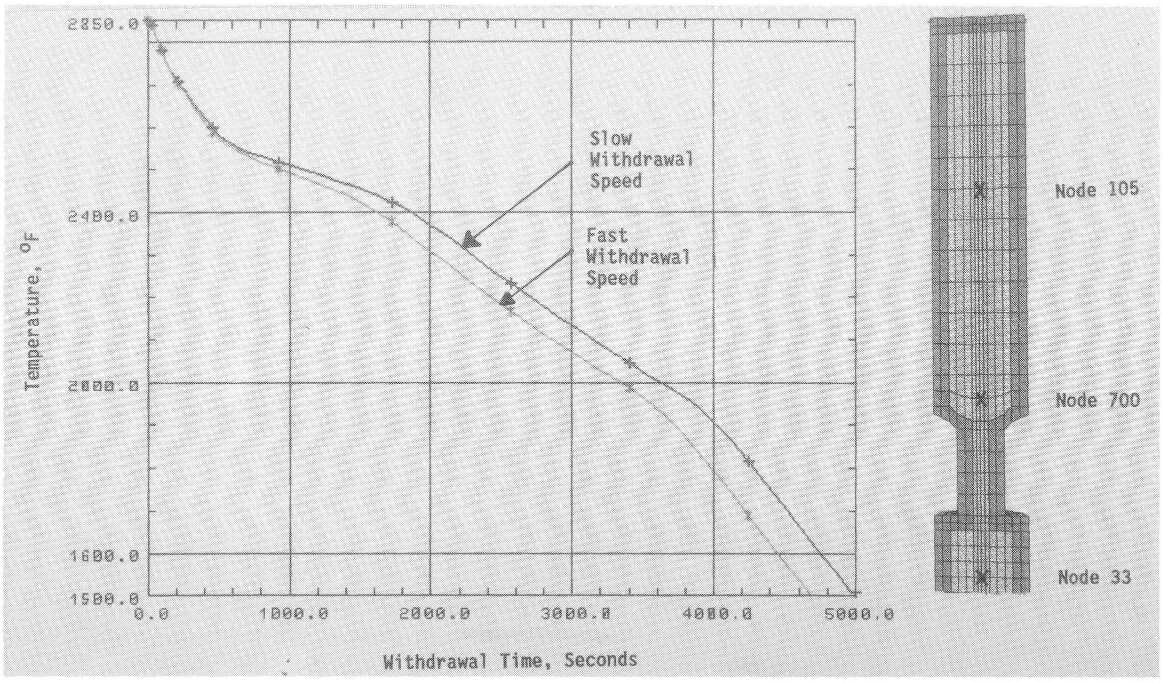

Fig. 11. Effect of withdrawal speed on cooling rate of Node 700 (see Fig. 7 for node location).

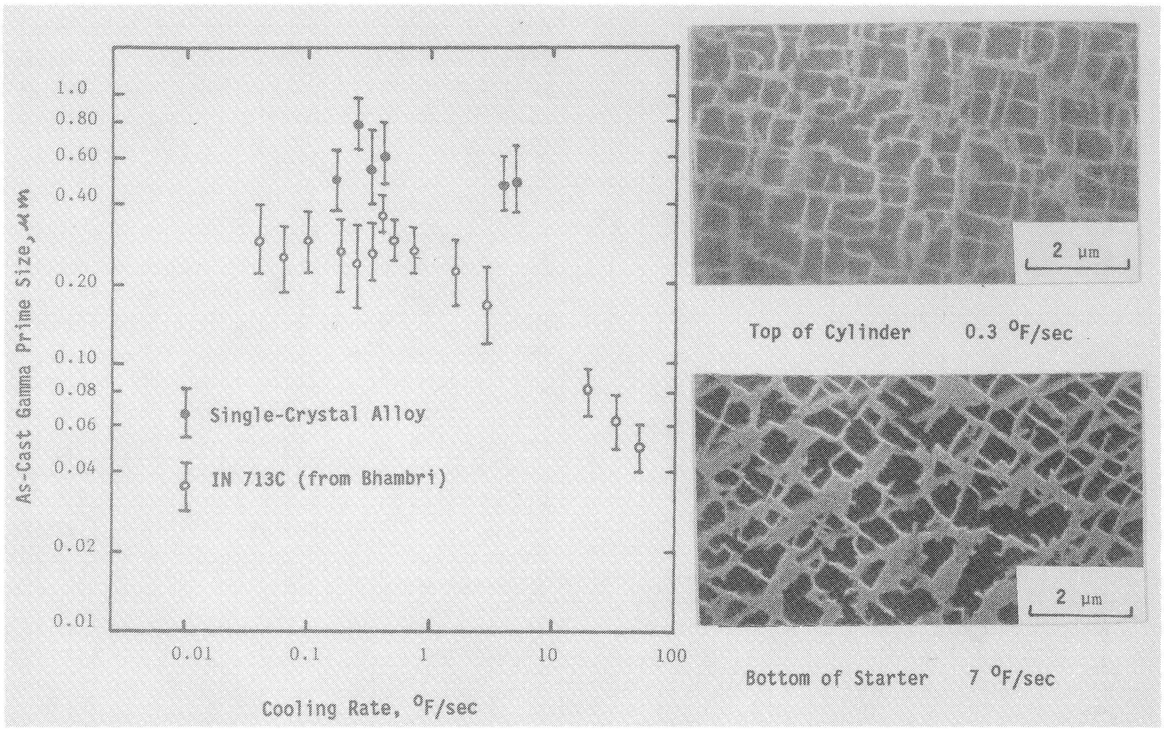

(A) (B)

Fig. 12 Measured as-cast gamma prime size as a function of calculated cooling rate.

of the castings. In general, the fineness[10] of DAS (both primary and secondary) is directly related to local solidification time or average cooling rate during solidification. As the heat is extracted faster from castings (i.e., shorter local solidification time or higher average cooling rate), the size of the resulted DAS and the degree of the associated microsegregation are also smaller.

Figures 13 and 14 show the measured primary and secondary DAS as a function of calculated local solidification time. The primary DAS was measured from transverse samples, and the secondary DAS was measured from longitudinal samples.[11]

Occurrence of Casting Defects

Table 1 shows the types of defect found from the experimental clusters cast in support of this work. The occurrence of freckles, equiaxed grains, and shrink is correlated with the temperature gradient (G) and solidification rate (R) to form a defect map, whereas the primary dendrite growth direction is predicted from the calculated shape of the mushy zone during solidification.

Table 1.
Types of Defects in Single-Crystal Castings

- Freckles *
- Recrystallized/Equiaxed Grains *
- Shrink *
- Off-Axis Primary Dendrites *
- Secondary-/Multi-Grains
- Slivers
- Low/High Angle Boundaries
- Cracks
- Misruns

* Predicted by Modeling

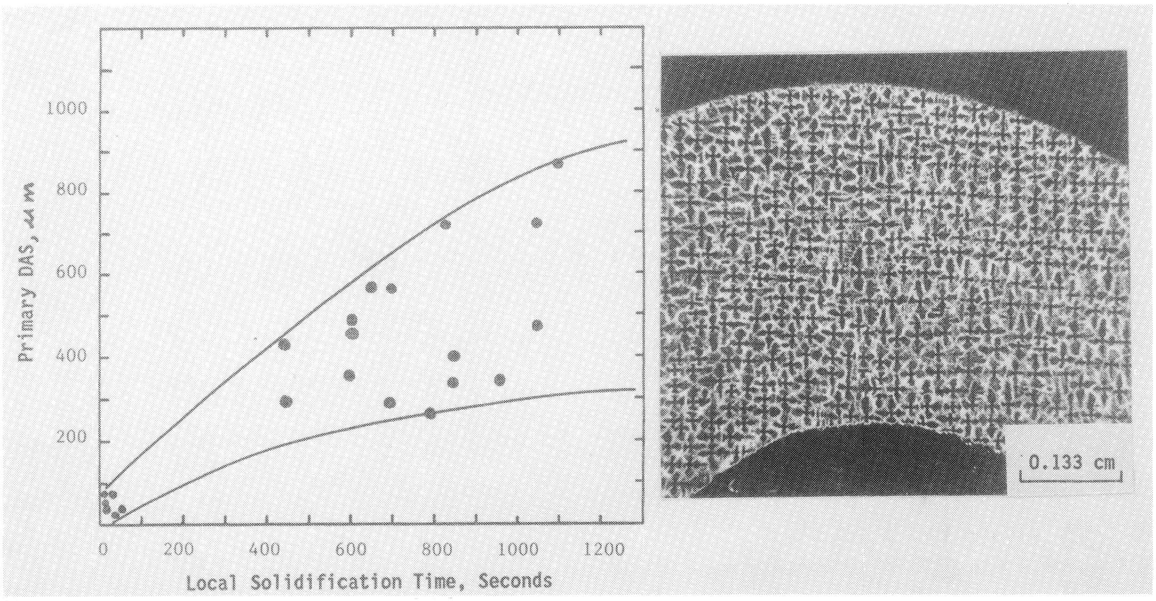

Fig. 13. Measured primary dendrite arm spacing of a single-crystal alloy as a function of calculated local solidification time.

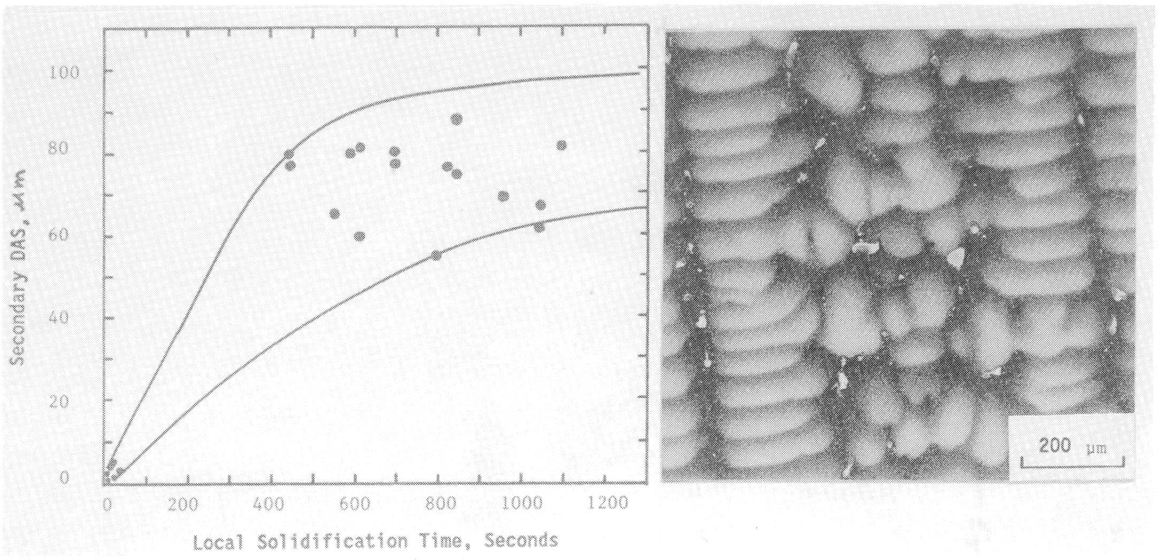

Fig. 14. Measured secondary dendrite arm spacing of a single-crystal alloy as a function of calculated local solidification time.

Freckles

Flemings and coworkers[12–18] have shown that the flow of solute-rich interdendritic liquid in the mushy zone during solidification is responsible for freckle-type macrosegregation. This interdendritic liquid moves as a result of solidification contraction, of gravity acting on a fluid of variable density, and of electromagnetic forces. Yu and coworkers[19–22] have also shown that freckles can be formed in VAR (vacuum arc remelting) and ESR (electroslag remelting) processed superalloy ingots.

Freckles in directionally solidified superalloys have been studied by Gell and Duhl and Copley et al.[24] Figure 15A is a schematic of the freckle formation mechanism in directionally solidified and single-crystal superalloys. Nickel-based superalloys usually contain aluminum and titanium to form the gamma prime strengthening phase based on $Ni_3(Al, Ti)$.

During the directional solidification process, solute elements such as Al and Ti are enriched in the liquid between dendrites near the bottom of the two-phase mushy zone adjacent to the solidified alloy. This Al- and Ti-enriched liquid has a lower density than both the average alloy and the liquid above the liquidus. The buoyancy due to the density difference results in jets of liquid rising to the top of the mushy zone. Meanwhile, solidification contraction results in jets of liquid moving downward to fill the solidification shrinkage. These moving jets can occasionally break off dendrite tips, which act as nuclei for chains of equiaxed grains, that is, freckles.

Gell and Duhl[23] showed that the formation of these moving jets is controlled by the difference between the liquidus and solidus temperatures (ΔT), the time required for the mushy zone to pass a point in casting (that is, local solidification time), the temperature gradient in the mushy zone (G) and the solidification rate (R). If there is a critical time, t_f^*, required to produce a detectable freckle trail, the cooling rate, $G \times R$, above which freckle formation will not occur is:

$$G \times R = \frac{\Delta T}{t_f^{\,*}} \tag{1}$$

Equation 1 is drawn in Figure 15B to show the cross-hatched area on the G versus the R plot where freckles should not occur.

The minimum cooling rate ($G \times R$) which will prevent freckle formation in the single-crystal castings of the present study can be obtained from the combination of experimental results and calculated cooling rates. Since no freckles were found in these cylinders, the lowest calculated $G \times R$ value represents the minimum cooling rate above which freckles will not form. When the cooling rate within the casting falls below this value, the freckle formation tendency of the casting will increase with a decrease of cooling rate. Figure 16 shows plots of average cooling rate contours for a solid cylinder.

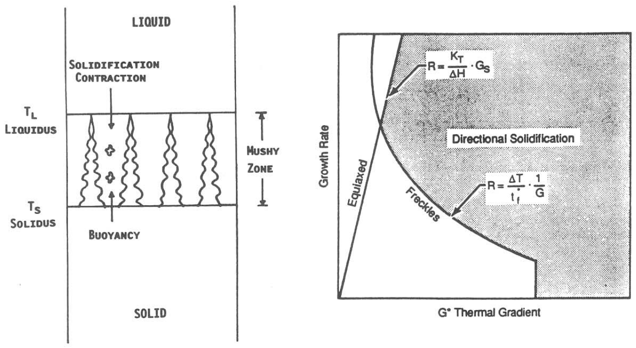

(A) (B)

Fig. 15. Schematic of solidification mechanism (A) and control theory (B) [23] *for the formation of freckles in directionally solidified and single-crystal superalloys.*

Equiaxed/Recrystallized Grains

During solidification, the solidification front morphology is controlled by the combination of the temperature gradient (G) in the liquid phase just ahead of the advancing interface, and by the interface velocity or solidification rate (R).[25] Figure 17A indicates the types of microstructures obtained within six nickel-based superalloys[2] directionally-solidified under a range of conditions with various values of G and R. The different solidification morphologies produced fall roughly into zones in the plot of G versus R that are consistent with the indicated transition lines between the zones, assuming that

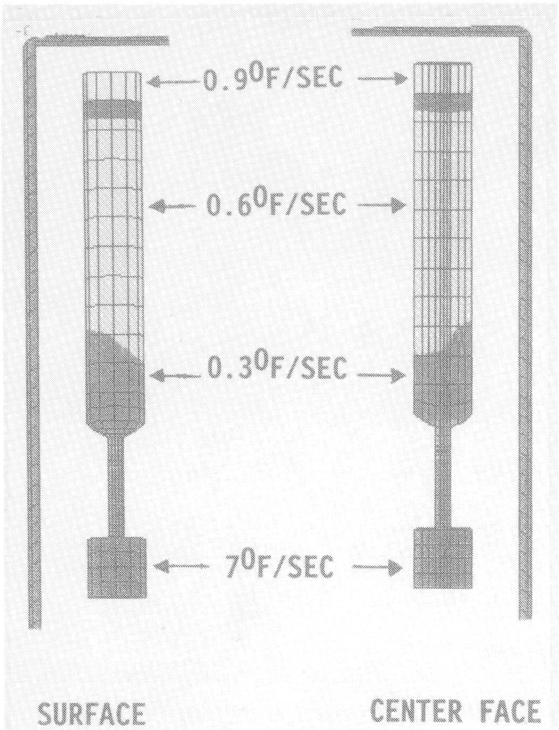

Fig. 16. Contour of average cooling rate for a solid cylinder.

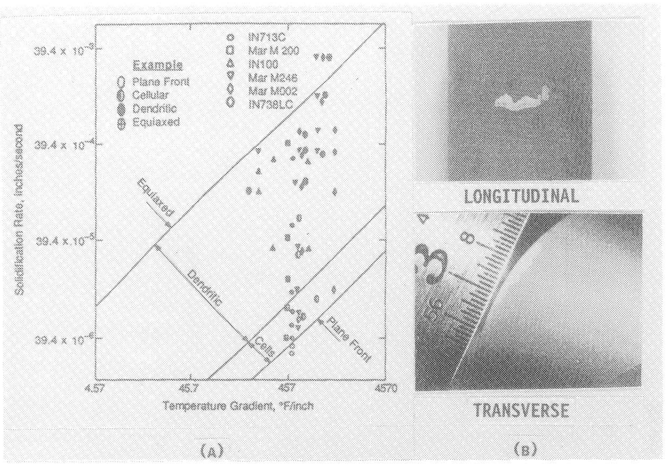

Fig. 17. (A) Solidification morphologies[2] *of directionally solidified single-crystal superalloys with various G and R values. (B) Recrystallized grain.*

G/R bands are similar for all nickel-based alloys. From the figure, it is possible to identify a different critical value of G/R for each solidification morphology transition.

Recrystallized grains[1] result from stress imparted to the casting either during the furnace withdrawal process or during post-solidification processing and handling. These grains nucleate during solution heat treatment and appear on the surface of the casting. Recrystallized grains can often be identified by the "twinning" seen in wrought grains. Both equiaxed and recrystallized grains can have depth similar to the diameter of the grain as seen on the surface.

Metallographic studies showed that only recrystallized grains (Fig. 17B) formed in these single-crystal castings during post-solidification handling and no equiaxed grains formed during casting. Thus, the lowest calculated G/R value is selected as the minimum G/R value above which equiaxed grains are not expected to form.

Shrink

Shrink is a common casting defect that occurs in the presence of metal contraction when feeding is restricted. Nickel-based superalloys contract on solidifying[26] and most of this contraction takes place while efficient feeding mechanisms (liquid and mass feeding) are still operative. However, since these alloys solidify in a mushy manner, mass feeding stops when the alloy is about 70% solidified. Capillary (that is, interdendritic and intergranular) feeding then becomes the only operative feeding mode. Microporosity (interdendritic shrink) formation occurs during the last stage of solidification when capillary feeding becomes insufficient.

Numerous investigations[27–31] have been conducted to define criterion functions for the prediction of shrink. The criterion function of shrink, f, introduced by Niyama et al.,[30] is widely accepted:

$$f = \frac{G}{\sqrt{T'}} = \frac{G}{\sqrt{GR}} = \sqrt{\frac{G}{R}} \qquad (2)$$

where G is the temperature gradient and T′ is the cooling rate in close vicinity to the solidus temperature. By calculating f everywhere in the casting, one may determine the location(s) where a critical f level will be approached. Regions in the casting below a critical f value may indicate microshrinkage.

Lecomte-Beckers[31] developed a theoretical model to estimate the microporosity formation propensity for directional solidified castings. A microporosity index, Δp, is developed to indicate the pressure drop resulting from the flow of fluid through the liquid-solid mushy zone. Higher Δp values indicate a poorer feeding condition and, hence, higher propensity for microporosity formation. The index can be expressed as:

$$\Delta p = \frac{24\mu\, \beta'\, n\, \tau^3 (T_L - T_S)}{\rho_L\, g} \cdot \frac{R}{G} \qquad (3)$$

where

μ = liquid viscosity,

$\beta' = \frac{(\rho_s - \rho_L)}{\rho_L{}'}$ where ρ_s and ρ_L are solid and liquid densities,

n = the number of interdendritic channels per unit area (related to primary DAS),

τ = tortuosity (related to secondary DAS),

T_L and T_s = liquidus and solidus temperatures, and

g = gravity.

The physical meaning of Equation 3 is that casting soundness is favored by a small solidification range, low dendrite number density and tortuosity, high residual liquid density and fluidity, high temperature gradient, and low solidification rate.

For the present study, G/R near the alloy's solidus temperature was selected as the criterion function for the prediction of shrink. A lower G/R value results in a higher tendency to form microporosity. Figure 18 is a calculated G/R map of a cylinder with core and shroud. It shows that the shroud region and the top surface of the starter have the lowest G/R values, which indicate these areas have the highest probability for the occurrence of shrink. This prediction is verified by the experimental castings.

Defect Map

Using the established defects formation criteria, a defect map based on G versus R plot can be constructed (Fig. 19). The construction of this defect map is essential because it facilitates the identification of solidification conditions that result in acceptable castings.

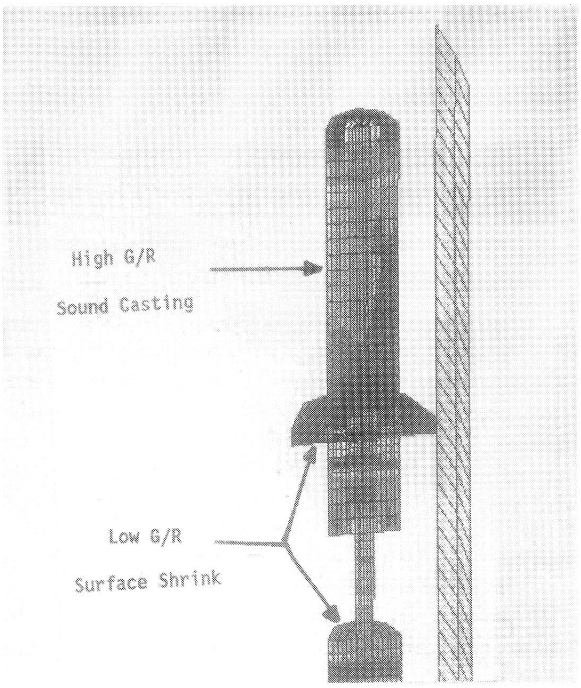

Fig. 18. Calculated G/R map of a cylinder with core and shroud.

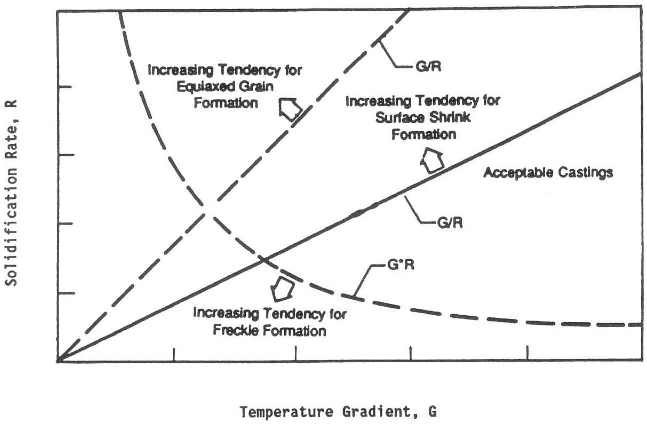

Fig. 19. Defect map based on G versus R plot.

Off-Axis Prediction of Primary Dendrite Direction

Single-crystal castings cast with grain selectors usually have <001> orientation aligned near parallel to the casting vertical stacking axis.[1] Because the dendrite growth direction is directly opposite to the heat flow direction, a poorly controlled heat flow condition can promote dendrite growth in directions that are not parallel to the <001> orientation. Laué X ray is used to inspect the overall dendrite growth direction (or crystallographic orientation) for the casting. The casting does not meet specifications when the angle between the primary dendrite direction and casting axis is greater than that specified by the design engineer.

Helical grain selectors usually result in castings that have <001> orientation aligned near parallel to the casting axis.[1] With the use of seed crystals, however, any required orientation can be achieved. Whether a seed crystal or a helical grain selector is used, solidification proceeds by growth of dendrites in the three <001> orientations, with the <001> orientation most closely aligned to the heat flow direction being the primary growth direction. In this study, helical grain selectors were used for all the castings.

After dendrites grow out of the grain selector, the primary growth direction of dendrites is controlled by the overall heat transfer condition in the casting. All sides of the casting should maintain approximately the same cooling rate so that the heat flow and, hence, the dendrite growth direction will be parallel to the casting stacking axis. If the heat transfer is such that one side (usually the side near the furnace wall) of the casting has a higher temperature gradient than the opposite side, the resulting heat flow direction will not be parallel to the casting stacking axis. Consequently, the magnitude of the angle between the primary dendrite direction and the casting stacking axis will increase, and the casting may be rejected.

Since the heat flow direction is perpendicular to the isotherms in the mushy zone, the casting primary dendrite growth direction can be estimated from the isotherm contour of the mushy zone. For a circular cluster configuration, the temperature distribution of the cylinder is symmetrical about the cluster radius that passes through the center of the cylinder (plane ABCD in Figure 20). This symmetry can be seen in Figure 21 (right), which also shows the small difference between temperatures at points F, G, and E in plane HIEF in the cluster circumferential direction. Consequently, the angle between the primary dendrite direction and the casting stacking axis in the cluster circumferential direction is near zero, and the primary dendrite direction only deviates from the casting stacking axis in cluster radial direction.

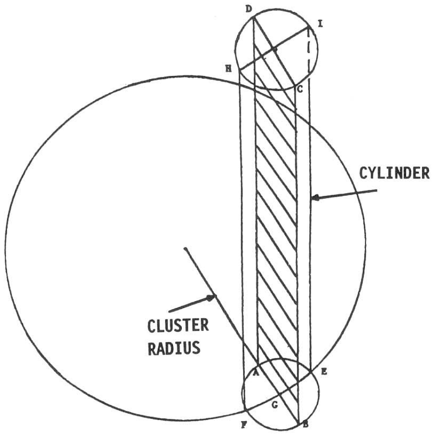

Fig. 20. Cylinder heat transfer condition for a circular cluster configuration.

In plane ABCD of Figure 20, the angle between the primary dendrite direction and the casting stacking axis, θ, can be estimated by:

$$\theta = 90 - \left(\frac{\theta_L - \theta_S}{2} \right) \quad (4)$$

where θ_L is the angle between the liquidus isotherm and casting axis, and θ_S is the angle between the solidus isotherm and the casting axis (Fig. 22). From Equation 4 and the casting isotherm contour shown in Figure 21, the estimated angle between primary dendrite direction and the casting stacking axis in the middle portion of Bar-2F is 6 degrees. This compares with an angle of 7 degrees that was measured from metallography (Fig. 22).

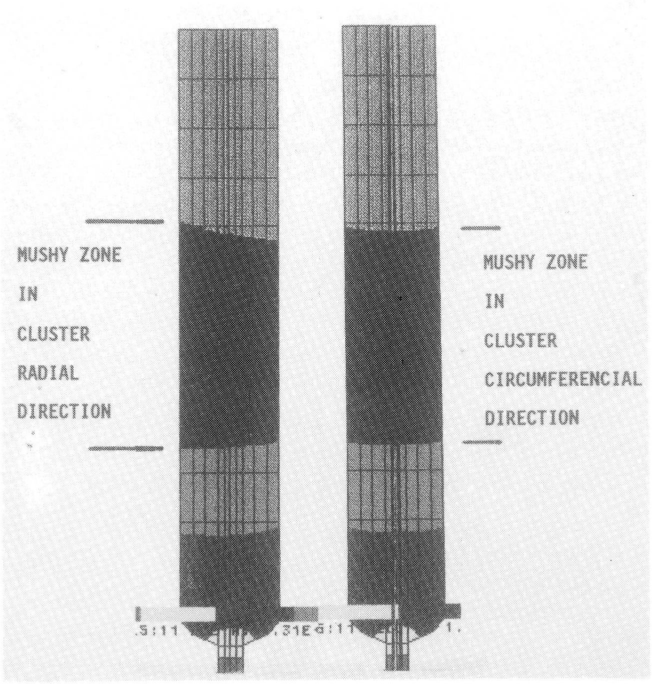

Fig. 21. Mushy zone shapes of a solid cylinder in cluster radial and circumferential directions.

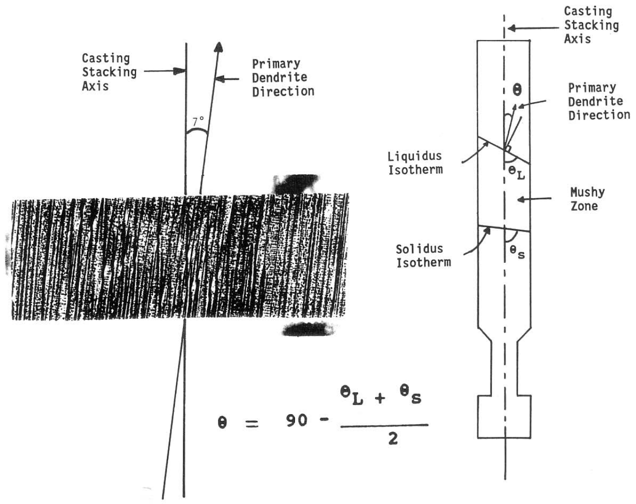

$$\theta = 90 - \frac{\theta_L + \theta_S}{2}$$

Fig. 22. Schematic for the prediction of the angle between the primary dendrite direction and the casting stacking axis.

Other Types of Defects

There are several other types of defects also found in single-crystal castings. They are slivers, secondary- and multi-grains, low/high angle boundaries, cracks, and misruns. The occurrence of these defects is not predicted by the current model. Efforts are being devoted to resolve this problem.

Slivers (Fig. 23) are grains forming streaks in the microstructure. They are usually aligned close to the primary direction, but misoriented in the transverse direction. Two possibilities have been proposed for the formation of slivers. One possibility assumes they form when the metal cooling rate G × R is above a critical value. The other possibility suggests that slivers nucleate from nonmetallic inclusions that contact with the metal.

Since the width of a sliver is usually about 1/8 in., it is very unlikely, from the heat transfer point of view, that the metal cooling rate during solidification of a small local area in the casting could be so significantly higher than the surrounding area as to cause grain nucleation. It seems more likely that inclusions serve as nuclei for these grains. Since the size of inclusions is small, and since the local heat transfer condition is similar to that of the surrounding area, the transverse dimension of a sliver is small and its longitudinal orientation will be close to the primary direction of the casting. Moreover, if an inclusion originates from the mold material, the sliver can be found by visual inspection of the casting surface. On the other hand, if a sliver nucleates from an inclusion that is located in the interior of the casting, it cannot be found by visual inspection unless the casting is cut and etched to show the transverse grain structure.

Secondary grains and multi-grains (Fig. 24A) usually occur when more than one grain emerges from the grain selector. Moreover, if the heat transfer condition during the solidification of a casting is such that one part of the casting (usually the shroud) cools much faster than the rest of the casting, secondary grains will nucleate and grow from the melt in competition with the primary grain. The best way to control the formation of secondary grains and multi-grains is to adjust the heat transfer conditions during withdrawal to ensure that all parts of the casting cool at about the same rate. This includes the careful control of heat transfer conditions at the grain selector region.

Low/high angle boundaries (Fig. 24B) may form during casting; the crystallographic orientation of the grain on each side of the boundary is different. This is acceptable only if the total misorientation is within specifications. These misaligned grains can appear as striations when they occur in clusters. Again, this condition could result from nucleation of secondary grains.

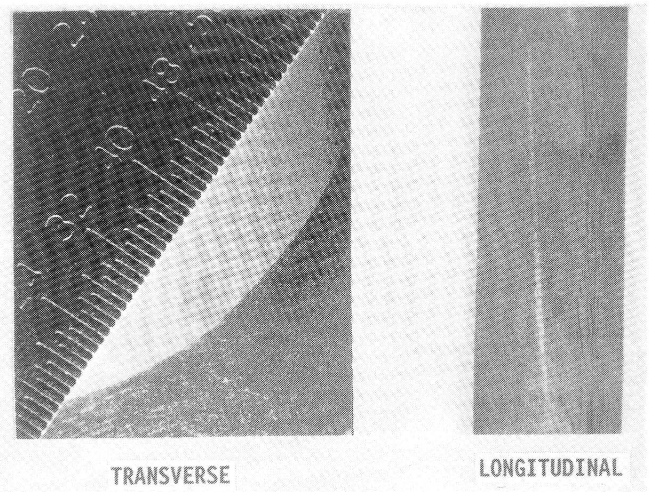

Fig. 23. Transverse and longitudinal views of a sliver in a directionally solidified single-crystal casting.

Cracks can be formed during solidification via hot tearing or after solidification due to excessive thermal stress. Figure 24C shows recrystallized grains near the cracking area, indicating the presence of thermal stress during crack formation, which must have occurred at lower temperatures.

Misruns (Fig. 24C) form when the initial metal temperature is so low that the metal does not fill the mold completely. Equiaxed castings usually have a higher tendency for the occurrence of misruns than directionally solidified and single-crystal castings. Control of the formation of cracks and misruns needs in-depth studies of hot tearing and thermal stress and the effect of mold filling and fluid flow on the initial metal temperature distribution.

CONCLUSIONS

The following conclusions can be drawn:

1. Finite-element modeling of the single-crystal investment casting process is an effective tool for aid in understanding and avoiding certain types of defects.
2. As-cast gamma prime size of the single-crystal alloy is about twice that of IN713C (an equiaxed alloy) and is approximately constant for cooling rates ranging from 0.3 to 7°F/sec.
3. The average casting cooling rate G × R in the mushy region should be higher than a critical value to avoid the formation of freckles. If the casting cooling rate is lower than this value, the tendency for freckle formation will increase.
4. G/R values near the alloy's liquidus temperature should be higher than a critical value to avoid the formation of equiaxed grains.
5. The casting G/R value near the alloy's solidus temperature should be higher than a critical value to avoid the presence of excessive surface shrink. If the G/R is lower than that value, the tendency for the formation of surface shrink will increase.
6. The primary dendrite growth direction to be estimated from the slope of the isotherm contours of the mushy zone. After dendrites grow out of the grain selector, the primary dendrite direction should be controlled by adjusting the heat transfer conditions so that all parts of the casting cool at about the same rate and the mushy zone isotherms remain perpendicular to the desired growth direction.
7. Defect map has been generated which serves as a powerful tool in predicting high integrity single-crystal castings.

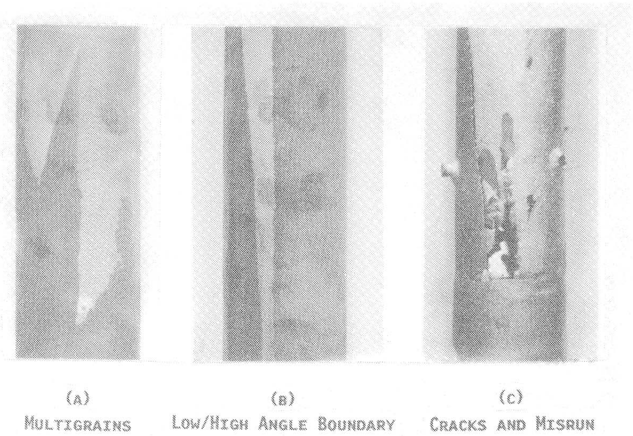

Fig. 24. Photographs of multi-grains (A), low/high angle boundaries (B), cracks and misruns (C) in directionally solidified single-crystal castings.

ACKNOWLEDGMENTS

This work was supported by contract No. F33615-85-C-5014 (GE Aircraft Engines is the primary contractor and PCC Airfoils is a subcontractor to GE Aircraft Engines) with the Air Force Wright Research and Development Center, Manufacturing Technology Directorate (WRDC/MT), Wright-Patterson AFB.

REFERENCES

1. D. N. Duhl; Superalloys II, pp 189–214, John Wiley Sons (1987).
2. M. McLean; *Directionally Solidified Materials for High Temperature Service*, The Metals Society, London (1983).
3. M. Gell, D.N. Duhl, and A.F. Giamei, *SUPERALLOYS 1980*, ASM, pp 205–214 (1980).
4. M. J. Beffel, J. O. Wilkes, and, R. D. Pehlke; "Finite Element Simulation of Casting Processes," *AFS Transactions*, vol 94, pp 757–764 (1986).
5. J. A. Dantzig, J. W. Wiese, K. Michalek and M. Robinson; "Application of ANSYS to Solidification Problems," ANSYS Users Conference (Apr 1985).
6. M. J. Beffel, K. O. Yu, M. Robinson, and K. R. Schneider; "Computer Simulation of Investment Casting Processes," *JOM*, vol 41, no. 2, pp 27–30 (Feb 1989).
7. A. K. Bhambri, T. Z. Kattamis, and J. E. Morral, *Met. Trans.*, 6B, p 523 *(1975)*.
8. B. J. Piearcey, B. H. Kear, and R. W. Smashey; *Trans. Q. ASM*, 60, p 634 (1967) .
9. *Aerospace Structural Metals Handbook*, Belfour Stulen, Inc. Code 4119, p 1, (1976).
10. R. Mehrabian; *Proceedings of the International Conference on Rapid Solidification Processing, Reston, Virginia, pp* 9–27 (Nov 13–16, 1977).
11. H. D. Bordy and A. F. Giamei; "Effect of Hafnium Additions on the Solidification Behavior of Directionally Solidified Superalloys", AFWAL-TR-81-4123, Contract No. F33615-75-C-5204, Final Report (Oct 1981).
12. M. C. Flemings and G. E. Nereo; T*rans. Met. Soc.*, AIME, vol 239, pp 1449–1461 (1967).
13. M. C. Flemings, R. Mehrabian, and G. E. Nereo; *Trans. Met. Soc.*, AIME, vol 242, pp 41–49 (1968).
14. M. C. Flemings and G. E. Nereo; *Trans. Met. Soc.*, AIME, vol 242, pp 50–55 (1968).
15. T. Fujii, D. R. Poirier, and M. C. Flemings; *Met. Trans. B.*, 10B, p 331 (1979).
16. C. L. Jeanfils, J. H. Chen, and H. J. Klein; *Proceedings of the Fourth International Symposium on Superalloys*, (1980).
17. S. Kou, D. R. Poirier, and M.C. Flemings; *Met. Trans. B*, vol 9B, p 771 (1978).
18. S. Kou, D. R. Poirier, and M. C. Flemings; *Electric Furnace Proceedings*, vol 35, p 221 (1977) .
19. K. O. Yu and H. D. Flanders; "Comparison of ESR-VAR Processes: Part II. Melting Phenomena and Ingot Structure," *Proc. of 1984 Vac. Melt. Conf. on Specialty Metals Melting and Process*, VMD-AVS, Pittsburgh, pp 107–118 (June 1984).
20. J. A. Domingue, K. O. Yu, and H. D. Flanders; "Characteristics of Macrosegregation in ESR IN-718," Symposium of Fundamentals of Alloy Solidification Applied to Industrial Processes, NASA, Cleveland, pp 139–149 (Sep 1984).
21. K. O. Yu, J. A. Domingue, G. E. Maurer, and H. D. Flanders; "Control of Macrosegregation in ESR and VAR Processed IN-718," *Proc. of the 8th International Conference on Vacuum Metallurgy*, Linz, Austria (Sep 1985).
22. K. O. Yu, J. A. Domingue, G. E. Maurer, and H. D. Flanders; "Macrosegregation in ESR and VAR Processes," *Journal of Metals*, vol 38, no. 1 (Jan 1986) pp 46–50.
23. M. Gell and D. N. Duhl; *Processing and Properties of Advance High Temperature Alloys*, S. Allen et al. editors, ASM, Metals Park, OH, p. 41 (1986) .
24. S. M. Copley, A. F. Giamei, S. M. Johnson, and M. F. Hornbecker, *Met. Trans.*, 1, p 2193 (1970).
25. M. Cohen, B. H. Kear and R. Mehrabian; *Proc. 2nd Int. Conf. on Rapid Solidification Processing*, Reston, Virginia, pp 1–23 (Mar 1980).
26. L. Quichou, F. Lavand, and G. Lesoult; "Superalloys 1980," *Proc. of the 4th Intern. Symp. on Superalloys*, J. K. Tien et al. editors, ASM, Metals Park, OH, p 205 (1980).
27. C. M Adams and H. F. Taylor, *AFS Transactions*, vol 61, p 686 (1953).
28. V. de L. Davies and R. Moe; *Solidification and Casting of Metals*, (Sheffield) Metals Society, London (1977).
29. A. Jeyarajan and R. D. Pehlke, *AFS Transactions*, vol 86, p 457 (1978).
30. E. Niyama, T. Uchida, M. Morikawa, and S. Saito; CIATF Paper No. 10 (1982).
31. J. Lecompte-Beckers; "Study of Microporosity Formation in Nickel-Base Superalloys," *Met. Trans. A.*, vol 19A, pp 2341–2348 (Sep 1988).